JNeurosci
THE JOURNAL OF NEUROSCIENCE

Research Articles | Cellular/Molecular

Disruption of the autism-associated Pcdh9 gene leads to transcriptional alterations, synapse overgrowth, and defective network activity in the CA1

https://doi.org/10.1523/JNEUROSCI.0491-24.2024

Received: 6 March 2024
Revised: 21 August 2024
Accepted: 17 September 2024

Disruption of the autism-associated *Pcdh9* gene leads to transcriptional alterations, synapse overgrowth, and defective network activity in the CA1

Abbreviated title: *Pcdh9* regulates synapse and network activity in the CA1

Federico Miozzo[1,2,*], Luca Murru[1,3], Greta Maiellano[4,5], Ilaria di Iasio[1], Antonio G Zippo[1,3], Annalaura Zambrano Avendano[1], Verjinia D. Metodieva[1,6], Sara Riccardi[1,7], Deborah D'Aliberti[8], Silvia Spinelli[8], Tamara Canu[9], Linda Chaabane[9], Shinji Hirano[10], Martien J. H. Kas[11], Maura Francolini[4], Rocco Piazza[8], Edoardo Moretto[1,3], Maria Passafaro[1,3,*]

[1] Institute of Neuroscience, CNR, Vedano al Lambro, Italy.

[2] Present address: Instituto de Neurociencias, Consejo Superior de Investigaciones Científicas, Universidad Miguel Hernández, Alicante, Spain.

[3] NeuroMI Milan Center for Neuroscience, University of Milano-Bicocca, Milan, Italy.

[4] Department of Medical Biotechnology and Translational Medicine, Università degli Studi di Milano, Milan, Italy.

[5] Present address: MeLis, CNRS UMR 5284, INSERMU1314, Institut NeuroMyoGène, Université de Lyon, Université Claude Bernard Lyon 1, Lyon, France.

[6] Present address: Neuroscience Research Center, Charité-Universitätsmedizin Berlin, corporate member of Freie Universität Berlin, Humboldt-Universität zu Berlin and Berlin Institute of Health, Berlin, 10117, Germany.

[7] Department of Life Sciences, University of Trieste, Trieste, Italy.

[8] School of Medicine and Surgery, Milano-Bicocca University, 20900 Monza, Italy.

[9] Preclinical Imaging, Experimental Imaging Centre, IRCCS-San Raffaele Hospital, Milano, Italy.

[10] Laboratory of Cell Biology, Faculty of Medicine, Kansai Medical University, Shinmachi 2-5-1, Hirakata City, Osaka, 573-1010, Japan.

[11] Groningen Institute for Evolutionary Life Sciences, University of Groningen, Groningen, The Netherlands.

* Corresponding author. fmiozzo@umh.es, maria.passafaro@in.cnr.it

Pages: 27

Figures: 5 main figures, 6 extended data figures and 6 extended data tables

Abstract: 230 words

Introduction: 491 words

Discussion: 1365 words

Conflict of interest statement

The authors declare no competing financial interests.

Acknowledgments

We thank the animal facility of the University Milano Bicocca for maintenance of mice colonies, Carlo Besta Neurological Institute for the use of the Transmission Electron Microscope, and the Experimental Imaging Centre of IRCCS-San Raffaele Hospital (Milano) for the MRI analysis. The financial support of Fondazione Cariplo, Italy (2019-3438) is gratefully acknowledged.

ABSTRACT

Protocadherins, a family of adhesion molecules with crucial role in cell-cell interactions, have emerged as key players in neurodevelopmental and psychiatric disorders. In particular, growing evidence links genetic alterations in Protocadherin 9 (*PCDH9*) gene with Autism Spectrum Disorder (ASD) and Major Depressive Disorder (MDD). Furthermore, *Pcdh9* deletion induces neuronal defects in the mouse somatosensory cortex, accompanied by sensorimotor and memory impairment. However, the synaptic and molecular mechanisms of *PCDH9* in the brain remain largely unknown, particularly concerning its impact on brain pathology. To address this question, we conducted a comprehensive investigation of PCDH9 role in the male mouse hippocampus at the ultrastructural, biochemical, transcriptomic, electrophysiological and network level. We show that PCDH9 mainly localizes at glutamatergic synapses and its expression peaks in the first week after birth, a crucial time window for synaptogenesis. Strikingly, *Pcdh9* KO neurons exhibit oversized presynaptic terminal and postsynaptic density (PSD) in the CA1. Synapse overgrowth is sustained by the widespread up-regulation of synaptic genes, as revealed by single-nucleus RNA-seq (snRNA-seq), and the dysregulation of key drivers of synapse morphogenesis, including the SHANK2/CORTACTIN pathway. At the functional level, these structural and transcriptional abnormalities result into increased excitatory postsynaptic currents (mEPSC) and reduced network activity in the CA1 of *Pcdh9* KO mice. In conclusion, our work uncovers *Pcdh9* pivotal role in shaping the morphology and function of CA1 excitatory synapses, thereby modulating glutamatergic transmission within hippocampal circuits.

SIGNIFICANCE STATEMENT

Converging evidence indicates that genetic alterations in Protocadherin 9 (*PCDH9*) gene are associated with Autism Spectrum Disorder (ASD) and Major Depressive Disorder (MDD). However, our understanding of *PCDH9* physiological role and molecular mechanisms in the brain, as well as its connection to synaptic dysfunction and brain pathology, remains limited. Here we demonstrate that *Pcdh9* regulates the transcriptional profile, morphology and function of glutamatergic synapses in the CA1, thereby tuning hippocampal network activity. Our results elucidate the molecular and synaptic mechanisms of a gene implicated in neurodevelopmental and psychiatric disorders, and suggest potential hippocampal alterations contributing to the cognitive deficits associated with these conditions.

INTRODUCTION

Synaptic connections among the approximately 90 billion neurons of the human brain must be established during neurodevelopment to give rise to functional neuronal circuitries. Failures during this process, leading to improper neuronal networks, result in neurodevelopmental and neuropsychiatric disorders. Cell adhesion molecules (CAMs) present on neuronal cell surface play a key part in neurodevelopment, regulating cell-cell recognition, cell adhesion and migration (Hirano and Takeichi, 2012). Among CAMs, protocadherin (PCDH) family counts more than 70 single membrane-spanning glycoproteins, representing the largest subgroup of the cadherin superfamily. PCDHs play critical roles in major neurodevelopmental processes, including neurite outgrowth, axon pathfinding, synapse formation and maturation (Peek, Mah and Weiner, 2017). Indeed, growing evidence links genetic alterations in *PCDH* genes to a wide range of brain pathologies (Flaherty and Maniatis, 2020; Mancini, Bassani and Passafaro, 2020).

Protocadherin 9 (*PCDH9*) gene has been associated with ASD after the identification of *de novo* and inherited copy number variations (CNVs) in autistic individuals (Marshall *et al.*, 2008; Bucan *et al.*, 2009). Furthermore, decreased *PCDH9* transcript levels were found in lymphoblasts of ASD patients (Luo *et al.*, 2012). Interestingly, meta-analysis of three genome-wide association studies (GWAS) linked the single nucleotide polymorphism (SNP) *rs9540720* in *PCDH9* gene with MDD and cognitive function impairment (Xiao *et al.*, 2018). *rs9540720* is predicted to lower *PCDH9* expression, and reduced *PCDH9* mRNA levels were found in MDD patients compared with healthy controls, thus leading to the identification of *PCDH9* as a susceptibility locus for MDD (Xiao *et al.*, 2018). A recent study also associated *PCDH9* with Essential Tremor (Clark *et al.*, 2022), a common movement disorder which is also characterized by cognitive and neuropsychiatric features (Lombardi *et al.*, 2001).

Pcdh9 KO mice display long-term social and object recognition deficits, hyperactivity and reduced sensorimotor competence. These behavioral abnormalities are accompanied by reduced cortical thickness of the somatosensory cortex, defective dendritic arborization and increased spine density of pyramidal neurons in these regions (Bruining *et al.*, 2015). A second study on a distinct *Pcdh9* KO line revealed further behavioral impairments including reduced fear extinction, possibly due to defects in *Ppp1r1b*$^{+}$ neurons of the basolateral amygdala (Uemura *et al.*, 2022). These investigations proved *Pcdh9* involvement in cognitive, sensory and emotional functions, thus strengthening the link with neurodevelopmental and psychiatric disorders. However, very little is known about the physiological role and molecular mechanisms of *Pcdh9* in the brain, and how its alteration relates to synaptic dysfunction and brain pathology.

Here, we examined *Pcdh9* levels and subcellular localization in the mouse brain. Then, we employed a combination of morphological, transcriptional and electrophysiological approaches to study *Pcdh9* function in the hippocampus in vivo. We show that *Pcdh9* depletion leads to aberrant pre- and postsynaptic morphology in the CA1, accompanied by dysregulation of synaptic genes expression. At the functional level, these alterations translate into abnormal excitatory transmission and disturbances in the hippocampal network activity. Collectively, our findings establish an important role for *Pcdh9* in the formation and function of CA1 glutamatergic synapses.

MATERIALS AND METHODS

Mice strains

Pcdh9 KO mice were obtained from Dr. Martien Kas' laboratory (University of Groningen, NL). Mice were maintained in rooms with 12 h light/dark cycles, temperature between 23-24 °C, and controlled humidity, with food and water provided *ad libitum*. Mice were housed at a maximum of five animals per cage in individually ventilated cages. All the experiments followed the guidelines established by the Italian Council on Animal Care and were approved by the Italian Government (protocol number 1152/2020-PR, 20/11/2020).

Immunocytochemistry

Primary neurons were prepared from cortices and hippocampi of Sprague-Dawley E18 rat brains as previously described (Zapata *et al.*, 2017). Neurons were plated onto coverslips coated overnight with poly-L-lysine at 75000 neurons per well, and grown in Neurobasal plus medium (Invitrogen) supplemented with 2% B27 plus (Invitrogen), 1% L-glutamine (Invitrogen), 1% penicillin/streptomycin (Invitrogen) and 10 mM Glutamate. Cultured neurons at DIV16-18 were washed in PBS and fixed in 4% paraformaldehyde, 10% sucrose for 15 min at room temperature (RT). After blocking/permeabilization in 10% normal goat serum (NGS), 0.1% Triton X-100, in PBS for 15 min at RT, neurons were incubated with primary antibodies (anti-PCDH9 Proteintech 25090-1-AP, 1:300; anti-PSD95 NeuroMab 75-028, 1:300; anti-HOMER1 Synaptic Systems 160004, 1:500 ; anti-GEPHYRIN Synaptic System 147021, 1:500; anti-VGLUT1 Synaptic Systems 135304, 1:200; anti-VGAT Synaptic Systems 131-003, 1:200) in GDB 1X solution (2X: 0.2% gelatin, 0.6% Triton X-100, 33 mM Na_2HPO_4, 0.9 M NaCl, pH 7.4) overnight at 4 °C. After three 10 min washes with high salt buffer (500 mM NaCl, 20 mM $NaPO_4^{(2-)}$, pH 7.4), the coverslips were incubated with secondary antibodies (anti-rabbit IgG Alexa-conjugated

488 Invitrogen A11029, 1:300; anti-mouse IgG DyLight-conjugated 649 Jackson Immuno Research 211-492-177, 1:300; anti-guinea pig IgG DyLight-conjugated 649 Jackson Immuno Research 706-175-148, 1:300) in GDB 1X solution for 1 h at RT. Neurons were washed three times with high salt buffer and incubated with DAPI (1:10000) for 5 min at RT. After washing with PBS for 5 min at RT, coverslips were mounted with Fluoromount (ThermoFisher Scientific).

Immunohistochemistry

One brain hemisphere from WT or *Pcdh9* KO mice was quickly washed in PBS and then drop fixed in 4% PFA in PBS for 24 h. The hemispheres were then washed for 72 h in PBS and subsequently cryoprotected in 30% sucrose in PBS. The hemispheres were then frozen in OCT and sectioned in 25 µm thick slices with a cryostat. Sections were then permeabilized using 1% and 0.3% Triton X-100 in PBS for 20 and 30 min, respectively, after which they were blocked with 20% NGS, 1% BSA and 0.3% Triton X-100 in PBS for 2 h at RT. Sections were incubated with primary antibodies (anti-MAP2 Synaptic Systems 188004, 1:500; anti-SHANK2 Synaptic Systems 162202, 1:1000; anti-CORTACTIN Abcam Ab81208 (EP1922Y), 1:1000) at 4 °C for 24 h in 20% NGS, 1% BSA and 0.3% Triton X-100 in PBS, after which sections were washed in 0.3% Triton X-100 in PBS for 30 min at RT. Sections were then incubated with secondary antibodies (anti-Guinea Pig Alexa-647 Invitrogen A21450; anti-Rabbit Alexa-488 Invitrogen A21206) in 20% NGS, 1% BSA and 0.3% Triton X-100 in PBS for 4 h at RT. After further washes in PBS for 10 min at RT, the sections were incubated with DAPI (1:10000) for 10 min at RT, washed in 0.3% Triton X-100 in PBS for 15 min, and mounted onto glass slides with Mowiol (Merck).

Image acquisition and analysis

For cultured neurons, fluorescence images were acquired with an LSM800 confocal microscope (Carl Zeiss) and a 63X oil-immersion objective (numerical aperture 1.4) with sequential acquisition setting, at 1024 x 1024 pixels resolution. Images were Z-series projections of approximately 6-10 images, taken at depth intervals of 0.75 µm. Co-localization analysis was performed on randomly selected dendrites using Fiji software (Schindelin *et al.*, 2012) with the plugin Jacop (Bolte and Cordelières, 2006). For Manders' colocalization coefficient, puncta were calculated by thresholding images at intensity equal to mean + 3 x St. Dev of the signals.

For the CA1 region, fluorescence images were acquired with an LSM800 confocal microscope (Carl Zeiss) and a 40X oil-immersion objective with sequential acquisition setting, at 2048 x 2048 pixels resolution. For each animal, images were acquired from 2 or 3 individual brain slices. Images were Z-series of approximately 10 images, taken at depth intervals of 0.8 µm. Single stacks were analyzed using Fiji, extracting the mean intensity of SHANK2 and CORTACTIN puncta that had an intensity greater than the mean + 3 x SD of the whole image intensity. The Z stacks were analyzed individually and then averaged to generate the values presented.

Membrane-enriched fractions preparation

Cortices and hippocampi were dissected from *Pcdh9* WT and KO 2-month-old animals, chopped with a razor blade in cold HEPES/sucrose buffer (4 mM HEPES pH 7.4, 320 mM sucrose) supplemented with protease inhibitor cocktails, incubated 10 min in ice and homogenized with a glass-teflon homogenizer. After centrifugation at 1000 g for 10 min at 4 °C, supernatants (S1) corresponding to total homogenate were centrifuged at 10000 g for 10 min at 4 °C. Resulting supernatants (S2) contained mainly cytosolic components while the pellet (P2) was enriched in membranes. After resuspension in HEPES/sucrose buffer, P2 fractions were centrifuged at 10000 g for 15 min at 4 °C to purify the preparation. P2 fraction were resuspended in modified RIPA buffer (50 mM TRIS-HCl, 200 mM NaCl, 1 mM EDTA, 1% NP40, 1% Triton X-100, pH 7.4) supplemented with protease inhibitor cocktail, and then quantified with bicinchoninic acid assay (BCA; Euroclone) prior to SDS-PAGE and Western blotting.

Electron Microscopy

2.5-month-old *Pcdh9* KO and WT male mice (2 mice per genotype) were deeply anesthetized with isofluoran before transcardial perfusion with EM Buffer (2.5% glutaraldehyde and 2% paraformaldehyde in 0.1 M sodium cacodylate buffer, pH 7.4). Brains were post-fixed in EM buffer for 24 hours at 4 °C. 100 µm slices were generated with a vibratome (Leica VT1000S) and the areas of interest manually dissected. Samples were then post-fixed with 2% osmium tetroxide, rinsed, *en-bloc* stained with 1% uranyl acetate, dehydrated using increasing concentration of ethanol and finally with propylene oxide and embedded in epoxy resin (Electron Microscopy Science, Hatfield, PA, USA). Thin sections (70 nm) were obtained with a EM UC6 ultramicrotome (Leica Microsystems, Austria), stained with a saturated solution of uranyl acetate in ethanol

20% and observed under a Tecnai G2 Spirit transmission electron microscope (TEM) (FEI, Eindhoven, Netherland). Profiles of excitatory synapse used for quantitative analyses were identified on the basis of three conditions: 1) the presence in their postsynaptic terminal of the electron-dense post-synaptic density (PSD); 2) the presence of a cluster of at least 3 synaptic vesicles in the pre-synaptic compartment 3) the presence of a defined synaptic cleft. Images were acquired at a final magnification of 37000X for the morphometric analysis and of 13500X for the analysis of synapse density using a Megaview (Olympus, Munster, Germany). Morphometric analyses were performed with Fiji software (Schindelin *et al.*, 2012) whereas, to evaluate synapse density, we used a stereological approach, as previously described (Colombo *et al.*, 2021).

Western blots

Samples were loaded on 9% polyacrylamide gels and then transferred onto nitrocellulose membranes (0.22 µm, GE Healthcare). Membranes were blocked in 5% milk, 0.1% TBS Tween-20 for 1 h at RT and then incubated with the primary antibodies (anti-PCDH9 home-made rat antibody (Asahina *et al.*, 2012), 1:2000; anti-GLUA1 Cell Signaling 13185S, 1:1000; anti-GLUA2/3 home-made rabbit antibody, kind gift from Cecilia Gotti, 1:3000; anti-GLUN2B Neuromab 75101, 1:1000; anti-VGLUT1 Synaptic System 135303, 1:15000; anti-GEPHYRIN ThermoFisher Scientific PA5-19589, 1:2000; anti-PICK1 Neuromab 75040, 1:2000; anti-PSD95 Cell Signaling 3450, 1:20000; anti-GAPDH Santa Cruz Biotechnology, 1:10000) in 0.1% TBS-Tween-20 overnight at 4 °C. After washing, the blots were incubated at room temperature for 1 h with horseradish peroxidase (HRP) - conjugated anti-rabbit (1:20000), anti-mouse (1:5000) or anti-rat (1:5000) antibodies in 0.1% TBS-Tween-20. Immunoreactive bands on blots were visualized by enhanced chemiluminescence (GE Healthcare). Quantification of bands intensity was performed with Fiji software (Schindelin *et al.*, 2012).

Hippocampal nuclei preparation and snRNA-seq sequencing

Hippocampal nuclei from two 2-month-old mice per genotype were prepared using Chromium Nuclei Isolation Kit (10X Genomics, PN-1000494) according to manufacturer instructions, with minor modifications. Briefly, hippocampi were dissected, flash-frozen in liquid nitrogen and immediately processed for nuclear preparation. Frozen hippocampi were dissociated in Lysis Buffer with pestle, passed onto Nuclei Isolation Column and resuspended in Debris Removal Buffer. Pelleted nuclei were washed twice in Wash and Resuspension buffer and passed twice through a 40 µm cell strainer (Greiner Bio-One EASYstrainer cell sieve 542040). Nuclei

integrity was examined at the confocal after DAPI staining, and the number of nuclei was estimated with a cell counting chamber. 13200 nuclei per sample were loaded on a Chromium instrument (10x Genomics). Libraries were prepared using a Single Cell 3' Kit with v3 Chemistry following a standard protocol. Library profile and concentration were assessed using a TapeStation (Agilent). Library concentration was also analyzed using a Qubit fluorometer. All the libraries were sequenced using a Novaseq 6000 (Illumina).

snRNA-seq analysis

Raw reads were processed with Cell Ranger v7.1. The raw single cell matrices were subsequently processed with Seurat v. 4.0.44 (Stuart *et al.*, 2019). Only nuclei with a number of detected genes between 500 and 4000, with less than 20000 unique reads/nucleus and less than 10% reads mapped to mitochondrial DNA were retained for subsequent analyses. Integration of different experiments was achieved using the SCTransform algorithm, while regressing out the effect of Unique Molecular Identifier (UMI) and mitochondrial counts. Principal Component Analysis (PCA) was performed as an initial dimensionality reduction step. All the components required to explain a cumulative variance of > 90% were retained for downstream processing, corresponding to the first 30 PCA components. Uniform Manifold Approximation and Projection (UMAP) algorithm was run on top of PCA to end-up with a total of 2 dimensions. These dimensions were subsequently used as input for cluster identification, which was performed with the Louvain algorithm. To optimize cluster resolution identification, the Clustree algorithm was applied, and the optimal cluster resolution was selected as a compromise between maximization of the SC3 stability index and cluster number. SingleR (Aran *et al.*, 2019) was subsequently applied to Log-Normalized gene counts at cluster level, using the CellDex dataset and the celldex::MouseRNAseqData as a reference to perform cell type identification, which was followed by direct manual curation. Differentially expressed genes were identified using a negative binomial generalized linear model. For each cluster, transcripts were considered to be differentially expressed in WT vs *Pcdh9* KO cells when the following three conditions were satisfied: absolute value of the $\log_2$FC KO/WT > 0.2, at least 10% of the cells expressing the transcript in at least one genotype, and a Bonferroni-adjusted p-value < 0.1. CA1 clusters were identified based on CA1 marker genes from Cembrowski et al. (Cembrowski *et al.*, 2016). For interactions and GO analysis, the DEG between the two genotypes found in CA1 clusters 5, 6 and 13 were combined in a unique list of CA1 DEG, from which *Pcdh9* was excluded. The interactions of the 31 CA1 DEG were explored with STRING (Szklarczyk *et al.*, 2019). GO analysis of the CA1 DEG was performed with gProfiler (Kolberg *et al.*, 2023) and SynGO (Koopmans *et al.*, 2019). STRING and SynGO analysis were performed on the human homologues of DEG. Genes were annotated as pre- and postsynaptic (Figure 3G)

based on SynGO ontologies. For GSEA (Reimand *et al.*, 2019), the complete list of genes detected in CA1 clusters 5, 6 and 13 was ranked by log_2FC(KO/WT) * -log_{10}p-value. As a gene set, the list of all human genes annotated as synaptic was used (GO:0045202; SynGO portal, Koopmans *et al.*, 2019), after conversion to their mouse homologues using Metascape (Zhou *et al.*, 2019). The genes coding for components of the excitatory and inhibitory PSD (Extended Data Figure 3-2B) were identified in Uezu et al. (Uezu *et al.*, 2016).

Behavioral assays

All behavioral tests were performed at a similar time of the day (1 to 3 hours before the light off) to avoid circadian effects. The mice were allowed to habituate to the behavioral room for at least 45 min before each test. Behavioral equipment was cleaned with 70% ethanol after each test session to avoid olfactory cues.

Social recognition test was performed as in Bruining et al. (Bruining *et al.*, 2015) (long-term SRE). Before testing all mice were group-housed. To avoid exposure to odor prior to testing, test and intruder animals were all housed in separate cages. The day before the test, intruder animals were labeled with neutral smelling waterbased markers. Habituation and testing took place in regular cages (29 x 17 x 11 cm) with fresh bedding. On day 1, 2-month-old males (test animals) were habituated in the test cage for 5 min and initially exposed to an age-matched male conspecific (familiar intruder) for 2 min. Then, test animals were returned to their home cage. On day 2, after 24 h, the test animal was habituated again in clean cage with fresh bedding for 5 min, and then exposed at the same time with the familiar intruder of day 1 and to a novel age-matched male (novel intruder) from a different cage than the familiar intruder. Social investigation was defined as the total time that the test mice engaged in social sniffing, anogenital sniffing and allogrooming. The time spent by the test animal in investigating each intruder was manually scored from video recordings by an observer blind to the animal's genotype.

For novel object recognition, habituation and testing took place in empty transparent plastic cages. The objects used were made of glass or plastic and were of sufficient height to discourage mice from climbing on the objects. In a pilot experiment, mice were exposed for 5 min to different couples of objects in order to select two that fulfilled the following conditions: mice had to show interest for both objects, with no overt intrinsic preference for one object compared to the other. The choice of which object to use as familiar and which one as novel was counterbalanced among the different animals tested. On day 1 and day 2, 2-month-old males were habituated in the test cage for 5 min. Then, test animals were returned to their home cage. On day 3, test animals were exposed to two identical objects (familiar objects) for 5 min, and then returned to their home

cage. On day 4, after 24 h, test animals were exposed for 5 min to the familiar object and to a novel object. Object exploration was defined as approaching and sniffing the object, or touching it with the forepaws. The time spent by the animals in investigating each object was manually scored from video recordings by an observer blind to the animal genotype.

In vivo Magnetic Resonance Imaging (MRI)

MRI experiments were conducted on a 7-Tesla scanner for rodents, fully equipped for brain MRI/MRS (Biospec, Paravision 6.0 Software Bruker-Biospin). A dedicated mouse head coil (4-channels) was used as receiver together with a volume coil as transmitter. A mixture of IsoVet (isoflurane 1-2%; Zootecnica, #104331020) with oxygen was used to anaesthetize animals and breath rate was constantly monitored to regulate the level of anesthesia. Body temperature was maintained through warm water circulating inside the bed. For cerebral anatomy analysis, T2 weighted MR images were acquired with coronal sections across the entire brain of 0.6 mm and an in-plane resolution of 71 µm (FOV = 16 × 14 mm, matrix = 224 × 200) using a fast-spin-echo sequence (TR/TE = 3500/44 ms, rare factor = 10, average = 10, 11 minutes of acquisition). T2-weighted images were analyzed using a MATLAB toolbox, the Atlas Normalization Toolbox using elastiX (ANTX, https://github.com/ChariteExpMri/antx2) (Koch *et al.*, 2019), allowing to extract the cerebral volume of different brain areas following the Allen Mouse Brain Atlas (http://mouse.brain-map.org/). Areas with a cluster of at least 5 voxels were considered that correspond to a minimum volume of 0.025 mm^3. Single brain region volume was then compared to the total brain volume of each mouse. The whole procedure was completed following the guidelines described in Koch et al. (Koch *et al.*, 2019).

RT-qPCR

mRNA was extracted from murine tissues using Nucleozol Reagent (Macherey Nagel, 15443435) following manufacturer's instructions. A total of 1 µg of extracted mRNA was used to synthetize cDNA using SuperScript™ VILO™ cDNA Synthesis Kit (Thermo Fisher). *Pcdh9* specific sequences were amplified from cDNA with SYBR Green PCR Master Mix (Applied Biosystems) using an Applied Biosystems 7000 Real-Time thermocycler. Parallel qPCR reactions were performed on *α-actin* as reference gene. Primers were designed with Primer-BLAST online tool (https://www.ncbi.nlm.nih.gov/tools/primer-blast/): *Pcdh9* exon 1 (F: ACCATCACCCAACTCTGACG, R: GGAGTGTATCCCACCGCATC), *Pcdh9* exon 2 (F:

AGACTGCCCTGGTAAGGGTT; R: AAGGAGGCATTCGGTCCAAG), *Pcdh9* exon 5 (F: CTCCTGGCTTGGGTCCATAC, R: GTGGCCGCCATTGTTGAAAT), *α-actin* (F: AGATGACCCAGATCATGTTTGAGA, R: CCTCGTAGATGGGCACAGTGT). Each reaction was performed in triplicate, and the results were analyzed using the ΔΔCT method.

Patch-Clamp

P25-P30 *Pcdh9* KO and WT male mice were humanely sacrificed and the brain was rapidly removed and placed in an ice-cold cutting solution containing: 195 mM sucrose, 10 mM NaCl, 25 mM $NaHCO_3$, 2.5 mM KCl, 1.25 mM NaH_2PO_4, 7 mM $MgCl_2$, 0.5 mM $CaCl_2$, 10 mM glucose (pH 7.3, equilibrated with 95% O_2 and 5% CO_2). Coronal slices from PFC and hippocampus (thickness, 250-350 µm) were prepared with a vibratome VT1000 S (Leica) and then incubated first for 40 min at 37 °C and then for 40 min at room temperature in artificial cerebrospinal fluid (aCSF), consisting of (in mM): 125 mM NaCl, 2.5 mM KCl, 1.25 mM NaH_2PO_4, 1 mM $MgCl_2$, 2 mM $CaCl_2$, 25 mM glucose, and 26 mM $NaHCO_3$ (pH 7.3, equilibrated with 95% O_2 and 5% CO_2). Slices were transferred to a recording chamber perfused with aCSF at a rate of ~2 ml/min at room temperature. Whole-cell patch-clamp electrophysiological recordings were performed with a Multiclamp 700B amplifier (Axon CNS molecular devices, USA) and using an infrared-differential interference contrast microscope. Patch microelectrodes (borosilicate capillaries with a filament and an outer diameter of 1.5 µm; Sutter Instruments) were prepared with a four-step horizontal puller (Sutter Instruments) and had a resistance of 3-5 MΩ. Miniature excitatory post synaptic currents (mEPSCs) and miniature inhibitory post synaptic currents (mIPSCs) were recorded from pyramidal neurons of the hippocampal CA1 region and the PFC (layers V/VI), as previously described (Murru *et al.*, 2021).

Field excitatory postsynaptic potential (fEPSPs) were evoked (0.05 Hz of frequency) and recorded from the stratum radiatum of the hippocampal CA1 stimulating the Schaffer Collaterals (SC) using aCSF-filled monopolar glass electrodes. Stimulus strength was adjusted to give 50% maximal response. fEPSPs were acquired at 20 kHz and filtered at 5 kHz. For paired pulse experiments, pairs of stimuli were delivered at 50 ms intervals every 20 s (frequency of 0.05 Hz) and paired pulse ratio (PPR) were calculated by dividing the slope of the second response for the first one. SC-CA1 long-term potentiation (LTP) was elicited using classic stimulation protocol (100 stimuli at 100 Hz) (Murru *et al.*, 2017). All the analyses were performed offline with Clampfit 10.1 software (Molecular Devices).

340

341 **Microelectrode Array (MEA)**

342 Extracellular recordings were carried out with HD-MEA system (BiocamX, 3Brain) using Arena HD-MEA chips
343 equipped with 4096 electrodes (21 × 21 μm^2 in size, 42 µm pitch). Hippocampal brain slices were obtained as
344 for Patch-Clamp experiments (400 µm thickness). Slice activity was recorded under continuous perfusion
345 (4.5 ml/min) in aCSF solution supplemented with the potassium channel blocker 4-Aminopyridine (100 µM,
346 Hello Bio). Recordings were performed at full-frame resolution (17855.5 Hz) and analyses of spikes rate, bursts
347 rate, bursts duration and spikes inside the burst were conducted off-line using dedicated python routines
348 (SpikeInterface) (Buccino *et al.*, 2020). When analyzing hippocampal slices, activated regions were manually
349 identified overlapping slice images taken with a stereomicroscope (Zeiss Stemi 305) and the pseudocolor
350 activity map visualized on the 3Brain software. For the analysis on the entire hippocampus, electrodes with a
351 spiking rate >0.05 spike/sec were considered and slices with less than 20 active channels were discarded.
352 The global synchronization index (SI) was calculated for each active channel as previously described (Kreuz
353 *et al.*, 2007). SI allows identifying clusters of locally synchronized neurons, and ranges from 0 (random
354 uncoordinated activity) to 1 (full synchronous activity).

355

356 **Statistical analysis**

357 Statistical comparisons were performed using GraphPad Prism software (San Diego, CA). The statistical
358 significance of differences between two groups was calculated using a nonparametric two-tailed Mann-
359 Whitney test. To compare three or more groups, Kruskal-Wallis followed by Dunn's multiple comparisons test
360 was used. Differences were considered significant at *p<0.05, **p<0.01, ***p<0.001, ****p<0.0001. n.s.
361 indicates not significant. Pairwise comparisons are shown as brackets.

362

363 **RESULTS**

364 **PCDH9 is enriched at glutamatergic synapses and its expression peaks in the postnatal hippocampus**

365 To examine *Pcdh9* function in vivo, we first determined its protein levels in the adult mouse brain by western
366 blot (WB) analysis. PCDH9 is widely present in the brain areas analysed, with a more prominent expression
367 in cortex and hippocampus, and undetectable in the other organs assessed, supporting a specific function for

PCDH9 in the central nervous system (Figure 1A, B). Then, we prepared hippocampal lysates from mice at different ages to study PCDH9 expression during neurodevelopment. We found that PCDH9 expression sharply increases at P7 and then progressively decreases and remains stable in the adult mouse (Figure 1C, D). The first three postnatal weeks are a critical time window for synapses formation and maturation (Li *et al.*, 2010), therefore PCDH9 up-regulation in this time window suggests a potential role in synaptogenesis. To study PCDH9 subcellular distribution, we performed cortex fractionation and mainly detected PCDH9 in the membrane-enriched fraction, as expected for a transmembrane protein (Figure 1E). In order to investigate PCDH9 localization at the synapse, we coimmunostained DIV18 cultures of cortical and hippocampal neurons for PCDH9 and presynaptic (VGLUT1, excitatory; VGAT1, inhibitory) or postsynaptic markers (PSD95, HOMER1, excitatory; GEPHYRIN, inhibitory) (Figure 1F and Extended Data Figure 1-1). PCDH9 was moderately enriched in the perinuclear region and clearly present in the neurites. Colocalization analysis (Figure 1G, H) revealed a broad overlap of PCDH9 and VGLUT1 signals, a moderate PCDH9 colocalization with VGAT1, PSD95 and HOMER1, and largely exclusive profiles with GEPHYRIN, indicating that PCDH9 is mainly present at excitatory synapses, predominantly in the presynaptic compartment. Taken together, these results indicate that PCDH9 is widely present in the brain, with a peak of expression in the hippocampus during the first postnatal weeks, and mainly localizes at excitatory synapses.

Pcdh9 **deletion leads to enlarged presynaptic and postsynaptic compartments in the CA1**

To understand *Pcdh9* function in vivo, we took advantage of *Pcdh9* KO mouse line (Bruining *et al.*, 2015). As an initial characterization, we performed MRI analysis on *Pcdh9* KO and WT brains. We found significant changes in the volume of multiple brain areas (Extended Data Table 2-1), suggesting that *Pcdh9* might play a role in neural proliferation, growth or migration, similarly to other Protocadherins (Mancini, Bassani and Passafaro, 2020).

Pcdh9 KO mice display impairments in social and object recognition (Bruining *et al.*, 2015). We could reproduce this evidence in our hands, thus confirming the robustness of the memory phenotype (Extended Data Figure 2-1A, B). Therefore, we decided to focus our study on the hippocampus, a quintessential region for memory (Lisman *et al.*, 2017). Moreover, hippocampal alterations have been largely documented in MDD (Duman, 2014) and ASD (Schumann *et al.*, 2004; Banker *et al.*, 2021), two pathologies associated with *PCDH9* in patients (Marshall *et al.*, 2008; Bucan *et al.*, 2009; Xiao *et al.*, 2018). Strikingly, ultrastructural analysis of excitatory synapses of the dorsal CA1 revealed a significant enlargement of the presynaptic terminal in *Pcdh9*

KO mice compared to WT animals (Figure 2A, B). As a consequence, the density of presynaptic vesicles was significantly reduced in *Pcdh9* KO neurons, while the pool of docked vesicles was unchanged (Figure 2A, B, and Extended Data Figure 2-2). Importantly, the overgrowth of the presynaptic terminal was paralleled by a concomitant increase in the length and surface of the postsynaptic density (PSD), and a non-significant augmentation of the spine head area (Figure 2A, B), indicating that both pre- and post-synaptic compartments are enlarged in *Pcdh9*-depleted neurons.

To understand whether *Pcdh9* role in synaptic structure was specific to CA1 or more general in the brain, we also examined the prefrontal cortex (PFC), another brain area strongly implicated in MDD and ASD (Hare and Duman, 2020; Mohapatra and Wagner, 2023). Examination of ventromedial PFC (vmPFC) synapses did not display any difference between the two genotypes, suggesting that the observed effect of *Pcdh9* KO on synaptic morphology is specific to CA1 (Figure 2C, D). Altogether, we showed that *Pcdh9* depletion leads to an aberrant size increase both in the presynaptic terminal and in the PSD, demonstrating that *Pcdh9* is important for establishing the correct morphology of CA1 excitatory synapses.

Pcdh9 deletion induces the dysregulation of key synaptic genes and the broad up-regulation of the synaptic transcriptome in the CA1

Then, we wanted to identify the molecular changes underlying the aberrant synaptic structure in the CA1 of *Pcdh9* KO mice. To this aim, we first performed a WB analysis of a panel of pre- and postsynaptic proteins. This approach did not reveal any obvious alterations in synapse composition between the two genotypes, either in the hippocampus or in the cortex (Figure 2E, F).

To gain a deeper insight into the molecular changes occurring in *Pcdh9*-depleted neurons, we conducted a single-nucleus RNAseq (snRNA-seq) experiment on 16833 cells from WT and *Pcdh9* KO hippocampi. Nuclei were separated into 46 clusters, that were assigned to neuronal and non-neuronal cell types (Figure 3A). Differentially expressed genes (DEG) analysis between *Pcdh9* KO and WT genotypes was implemented for each cluster. Surprisingly, *Pcdh9* was identified as an up-regulated DEG in *Pcdh9* KO neurons across multiple clusters. This was due to the increased transcription of *Pcdh9* locus downstream of the deleted exon 2, as verified by RT-qPCR (Extended Data Figure 3-1A). No full-length or truncated PCDH9 protein was detected in *Pcdh9* KO hippocampal lysates after WB with antibodies targeting PCDH9 C-terminal region, confirming the full knock-out of the protein (Extended Data Figure 3-1B).

Taking advantage of established CA1 marker genes (Cembrowski *et al.*, 2016), we identified 7 cell clusters containing CA1 excitatory neurons (Figure 3B, C). Among the CA1 clusters, *Pcdh9* disruption led to the differential expression of 15, 21 and 4 genes in clusters 5, 6 and 13, respectively (Figure 3D and Extended Data Table 3-1, 3-2). Importantly, GO analysis of the combined 31 DEG from the three aforementioned CA1 clusters (Figure 3E and Extended Data Table 3-3) found enriched categories related to synapse and cell junction (Figure 3F and Extended Data Table 3-4). In agreement, based on SynGO database for synapse ontology (Koopmans *et al.*, 2019), multiple DEG were annotated as synaptic genes, mostly related to the postsynaptic compartment (Figure 3G and Extended Data Table 3-5). Notably, multiple up-regulated DEG are known to promote spine formation. These include the PSD scaffold *Shank2*, a critical regulator of spine shape (Sarowar and Grabrucker, 2016), the PSD components *Cttn* and *Csmd2* required for spine and dendrite morphogenesis (MacGillavry *et al.*, 2016; Gutierrez, Dwyer and Franco, 2019), and the kinases *Camk2a* and *Dapk1* which act in structural synaptic plasticity (Canal *et al.*, 2011; Goodell *et al.*, 2017). It is remarkable that the top up-regulated gene across the CA1 clusters is the non-coding RNA *Bc1*. *Bc1* has been previously implicated in the modulation of spine head and PSD size (Briz *et al.*, 2017), therefore its dysregulation could also be implicated in the impaired synaptic organization of *Pcdh9*-depleted neurons. To validate our transcriptomic analysis at the protein level, we immunostained hippocampal sections from WT and *Pcdh9* KO mice for the protein products of *Cttn* (CORTACTIN) and *Shank2* (SHANK2). Importantly, we found that both CORTACTIN and SHANK2 levels are significantly increased in *Pcdh9* KO CA1 neurons compared to WT (Figure 3H, I), in agreement with *Cttn* and *Shank2* up-regulation detected by snRNA-seq.

Despite the number of DEG reaching statistical significance in CA1 clusters was relatively small, we noticed that a large majority of genes showed a moderate up-regulation in *Pcdh9* KO neurons compared to WT (Figure 3D). We asked whether this global up-regulation was driven by synaptic genes, or rather general across all gene categories. Remarkably, pre- and postsynaptic genes showed a KO/WT fold change significantly higher than the rest of the transcriptome in CA1 clusters (Figure 3J). Accordingly, Gene Set Enrichment Analysis (GSEA) revealed the up-regulation of synaptic genes across gene expression data of CA1 clusters (Extended Data Figure 3-2A). In particular, genes coding for proteins localized to excitatory synapses showed a more pronounced up-regulation compared to genes related to inhibitory synapses (Extended Data Figure 3-2B). Overall, our snRNA-seq approach revealed that *Pcdh9* ablation leads to the dysregulation of key regulators of synapse size, and to a moderate but broad up-regulation of the synaptic transcriptome, thus sustaining the overgrowth of the pre- and postsynaptic compartments in CA1 excitatory synapses.

457

458 ***Pcdh9* deletion causes alterations in glutamatergic transmission and defective network activity in the**
459 **CA1**

460 Next, we asked how the synaptic and molecular alterations induced by *Pcdh9* depletion would impact on
461 neuronal function. Electrophysiological recordings on pyramidal neurons from dorsal CA1 acute slices
462 revealed a significant increase in the frequency of miniature excitatory postsynaptic currents (mEPSCs) in
463 *Pcdh9* KO CA1, which doubled compared to WT (Figure 4A, B). This alteration was specific to excitatory
464 currents, as recording of miniature inhibitory postsynaptic currents (mIPSCs) did not reveal any difference
465 between genotypes, despite a trend towards reduced mIPSCs frequency in *Pcdh9* KO neurons was observed
466 (Extended Data Figure 4-1A, B). In agreement with electron microscopy observations, no differences in
467 mEPSCs properties between genotypes were observed in vmPFC slices (Figure 4C, D). The change in
468 mEPSCs frequency could originate from presynaptic alteration in glutamate release, therefore we performed
469 paired-pulse ratio (PPR) experiments. No alterations in glutamate release probability were observed in *Pcdh9*
470 KO mice (Figure 4E), suggesting that a postsynaptic rather than a presynaptic defect might underlie the
471 alteration in mEPSCs frequency. Next, we examined whether *Pcdh9* KO impaired long-term potentiation (LTP).
472 Field excitatory post-synaptic potentials (fEPSPs) responses were recorded before and after high-frequency
473 stimulation (HFS). No difference was found between the two genotypes, indicating that *Pcdh9* deletion does
474 not affect this form of synaptic plasticity (Figure 4F). In conclusions, we found that *Pcdh9* disruption leads to
475 enhanced glutamatergic transmission, likely due to postsynaptic mechanisms.

476 Finally, we investigated the hippocampal network activity from *Pcdh9* KO and WT hippocampal slices using
477 high resolution microelectrode array (MEA) (Figure 4G). Quantification of firing rate, burst activity, number of
478 spikes per burst and burst duration in the whole hippocampus did not reveal any difference between WT and
479 *Pcdh9* KO genotypes (Extended Data Figure 4-1C). However, multivariate ANOVA (MANOVA) test of these
480 combined four features indicated a significant difference between the two genotypes ($p = 0.009$), suggesting
481 that *Pcdh9* ablation might lead to disturbances in the hippocampal circuits. Therefore, we examined the
482 network activity within each of the different hippocampal subregions separately. Remarkably, we found a
483 significant decrease of firing rate and burst activity specifically in the CA1, but not in the CA3 or DG, of *Pcdh9*
484 KO animals (Figure 4H, I). Furthermore, *Pcdh9*-depleted CA1 displayed a decrease in the synchronization
485 index (SI) (Figure 4J). Altogether, these results indicate that the structural, transcriptional and functional

synaptic alterations induced by *Pcdh9* deletion at the neuronal level, are accompanied by a reduction in CA1 network activity and synchronization (Figure 5).

DISCUSSION

In this study, we explored the physiological role of *Pcdh9* in CA1 synapses. First, we determined that PCDH9 localizes at excitatory synapses, predominantly in the presynaptic compartment, with an expression peak in the first postnatal week. Second, we combined ultrastructural, biochemical, transcriptional, and electrophysiological approaches to characterize excitatory synapses in *Pcdh9* KO mice. One of the most striking findings of our work is that *Pcdh9* deletion leads to synapse overgrowth in the CA1. Previous studies have implicated other protocadherins in spine generation or elimination (Mancini, Bassani and Passafaro, 2020), but their role in shaping synapse morphology has received less attention. Minor changes in synaptic structural features were reported in *Pcdh17* KO and *Pcdh19* mosaic mice (Hoshina *et al.*, 2013; Giansante *et al.*, 2023). Here we show that *Pcdh9* ablation causes the aberrant enlargement of both presynaptic and postsynaptic compartments, demonstrating *Pcdh9* requirement for the control of synaptic size in the CA1. In rodents, synapses acquire their typical structure with normal sized synaptic vesicles and postsynaptic thickening at P7 (Rice and Barone, 2000; Li *et al.*, 2010). Our observation that PCDH9 hippocampal levels peak at P7, in line with analogous findings in the somatosensory cortex (Bruining *et al.*, 2015), supports the conclusion that *Pcdh9* plays a role in synapse maturation. Therefore, we speculate that the synaptic alterations observed in *Pcdh9* KO CA1 originate during postnatal neurodevelopment, and are then maintained in the adult brain.

Regarding synaptic density, we did not observe any change in the dorsal CA1 of *Pcdh9* KO mice, while previous reports found an increased spine number in the somatosensory cortex of these animals (Bruining *et al.*, 2015), and reduced spine counts in the ventral CA1 of a distinct *Pcdh9* KO line (Uemura *et al.*, 2022). Collectively, this suggests that *Pcdh9* role in spine generation is highly specific to the brain regions considered, possibly depending on the particular *Pcdh9* expression profile and PCDH9 protein interactors in the different brain areas.

Thanks to our single-nucleus transcriptional analysis, we gained insights into the molecular changes underlying synapse overgrowth in *Pcdh9* KO neurons. First, we noticed that most genes showed a mild up-regulation in *Pcdh9* KO neurons compared to WT. Remarkably, this global trend towards increased transcriptional levels

was driven by synaptic genes: taken collectively, pre- and postsynaptic genes were up-regulated much more strongly than non-synaptic genes. This moderate but broad up-regulation of synaptic components could sustain the overgrowth of presynaptic terminal and PSD observed in *Pcdh9* KO neurons. Second, in *Pcdh9* KO neurons we identified several up-regulated DEG which are known to promote synapse growth, such as *Shank2*, *Cttn*, *Camk2a*, *Dapk1* and *Csmd2*. The PSD scaffold *Shank2* recruits the actin-regulator *Cttn* to control actin dynamics and stimulate synapse morphogenesis (Sala *et al.*, 2001; Steiner *et al.*, 2008; MacGillavry *et al.*, 2016), and *Shank2* deficiency leads to a reduction in PSD thickness in the CA1 region (Pappas *et al.*, 2017). Therefore, our results showing the concomitant increase in *Shank2* and *Cttn* levels in *Pcdh9* KO CA1, both at the transcriptional and protein levels, strongly point to the SHANK2/CORTACTIN pathway as a primary mechanism driving synapse overgrowth in *Pcdh9* KO neurons. Furthermore, *Camk2a* promotes activity-dependent spine enlargement by recruiting the actin cytoskeleton (Curtis *et al.*, 2023), and *Dapk1* functions in structural synaptic plasticity by regulating *Camk2a* binding to the NMDA receptor (NMDAR) subunit GluN2B (Goodell *et al.*, 2017). Also, The PSD component *Csmd2* promotes the development and maintenance of dendrites and synapses (Gutierrez, Dwyer and Franco, 2019). Therefore, the coordinated up-regulation of the *Shank2*/*Cttn* and *Camk2a*/*Dapk1* pathways, along with increased *Csmd2* gene levels, are likely responsible for the synaptic overgrowth observed in *Pcdh9* KO neurons.

Further studies are needed to clarify how *Pcdh9* deletion mechanistically leads to the transcriptional dysregulation of synaptic genes. Beyond their role as adhesion molecules, Protocadherins also function as signaling hubs by regulating multiple intracellular cascades, including pathways controlling gene expression such as *Wnt*/*ß-catenin* (Pancho *et al.*, 2020). Moreover, a recent report unveiled a direct role for PCDH9 in the repression of gene transcription in gastric cancer cells, through the interplay with the DNA methylation machinery (Zhang *et al.*, 2024). Thus, PCDH9 signaling might negatively modulate the transcription of synaptic genes, which could explain their up-regulation in *Pcdh9*-ablated neurons. Proteomic studies would be instrumental to determine PCDH9 interactors and identify the signaling axis dysregulated in *Pcdh9* KO neurons.

Our snRNA-seq approach unveiled gene expression alterations in other neuronal and non-neuronal clusters besides CA1. DEG in these clusters only partly overlap with those identified in CA1 neurons, possibly suggesting cell-type specific effects of *Pcdh9* deletion. Further research is needed to assess *Pcdh9* role in other hippocampal regions and cell types.

Through patch-clamp recording, we found that *Pcdh9* disruption positively modulates excitatory transmission. Considering that neither the pool of synaptic vesicles nor their release probability was increased in *Pcdh9* KO mice, we hypothesize that the augmented mEPSCs frequency originates from alterations in the postsynaptic compartment. In agreement, we revealed increased levels of several PSD components and key regulators of glutamatergic transmission, such as *Shank2* and *Camk2a*. The SHANK family proteins function as scaffold at the PSD of excitatory synapses (Jiang and Ehlers, 2013), and their dysregulation causes alterations in postsynaptic currents (Peça *et al.*, 2011; Duffney *et al.*, 2013; Pappas *et al.*, 2017). Moreover, enhanced CaMK2a activity has been proven to alter glutamatergic transmission by reducing the proportion of silent synapses in the CA1 (Poncer, Esteban and Malinow, 2002) or modifying AMPA receptors gating properties (Kristensen *et al.*, 2011). Therefore, we believe that the augmented levels of these genes might underlie the increased mEPSCs frequency in *Pcdh9*-depleted CA1 neurons. Furthermore, we observed a downward trend for mIPSCs frequency in *Pcdh9* KO neurons, which could also contribute to the positive modulation of excitatory transmission.

While *Pcdh9* depletion increases the frequency of excitatory currents in CA1 neurons, MEA analysis revealed that the resulting CA1 network paradoxically exhibits a global reduction of neuronal activity and synchronization. Although we cannot provide a comprehensive mechanistic explanation for our observations, multiple factors could account for the contrasting electrophysiological changes at the network and single-neuron levels. First, the most strongly and significantly up-regulated DEG in *Pcdh9* KO CA1 neurons is the non-coding RNA *Bc1*. Intriguingly, *Bc1* KO mice exhibit increased brain activity in the cortex and prolonged synchronized discharges in the hippocampus (Zhong *et al.*, 2009; Briz *et al.*, 2017). Therefore, it is reasonable to hypothesize that *Bc1* up-regulation might induce an opposite effect, thus contributing to the observed reduction in CA1 network activity and synchronization in *Pcdh9* KO mice. Second, Protocadherins are recognition molecules essential for neuronal wiring during neurodevelopment (Peek, Mah and Weiner, 2017; Mancini, Bassani and Passafaro, 2020). It is then conceivable that *Pcdh9* deletion might lead to inappropriate assembly of hippocampal circuitries, resulting into defective network activity. Finally, it is worth underling that contrasting electrophysiological effects at the single neuron and network levels were previously described for other synaptic proteins (Giansante *et al.*, 2023; Lee *et al.*, 2024). In particular, Giansante and colleagues showed increased neuronal excitability and reduced network activity in a mouse line carrying the mosaic deletion of another Protocadherin family member, *Pcdh19*. This aspect further highlights the complex nature of Protocadherin-related synaptic regulation.

Growing evidence from human neuropathological studies and animal models indicate that autism may be conceptualized as a disease of the synapse (Toro *et al.*, 2010), especially of the glutamatergic ones (Moretto *et al.*, 2018). Post-mortem research on ASD individuals revealed an increase in spine density of cortical pyramidal neurons (Hutsler and Zhang, 2010). Furthermore, multiple genes regulating PSD organization have been associated with ASD and intellectual disabilities (Toro *et al.*, 2010; Penzes *et al.*, 2011). To this regard, our findings are of great interest, as they reveal that disruption of the autism associated gene *Pcdh9* leads to aberrantly enlarged CA1 synapses and dysregulation of genes controlling synaptic size. Notably, 5 DEG identified in this work (*Camk2a*, *Dnmt3a*, *Galnt9*, *Pabpc1* and *Shank2*) are present in the SFARI database for ASD risk genes. Further research is required to examine whether ASD patients present dysmorphic synapses in the CA1.

In summary, our multi-level study sheds light on *Pcdh9* as a novel regulator of CA1 excitatory synapses size and function, with relevant implications for hippocampal circuits activity.

FUNDING

Fondazione Cariplo, Italy (2019-3438)

AUTHOR CONTRIBUTION

F.M. and A.Z.A. performed the biochemical analysis. I.D.I, E.M and V.M. performed the stainings. F.M. and S.R. performed the behavioral tests. G.M. and M.F. performed and supervised the EM analysis, respectively. F.M., D.D. and S.S. performed the snRNA-seq. F.M. and R.P. analyzed snRNA-seq data. L.M. performed and analyzed the electrophysiological recordings. L.M. and A.Z. performed and analyzed MEA recordings, respectively. T.C. and L.C. performed the MRI study. S.H. and M.K. provided experimental tools. F.M. prepared all the figures and wrote the manuscript. M.P. conceptualized the study, acquired funding, and reviewed the manuscript. All authors reviewed and edited the manuscript.

598 **RFERENCES**

599 Aran, D. *et al.* (2019) 'Reference-based analysis of lung single-cell sequencing reveals a transitional profibrotic
600 macrophage', *Nature Immunology*, 20(2), pp. 163–172. Available at: https://doi.org/10.1038/s41590-018-
601 0276-y.

602 Asahina, H. *et al.* (2012) 'Distribution of protocadherin 9 protein in the developing mouse nervous system',
603 *Neuroscience*, 225, pp. 88–104. Available at: https://doi.org/10.1016/j.neuroscience.2012.09.006.

604 Banker, S.M. *et al.* (2021) 'Hippocampal contributions to social and cognitive deficits in autism spectrum
605 disorder', *Trends in Neurosciences*, 44(10), pp. 793–807. Available at:
606 https://doi.org/10.1016/j.tins.2021.08.005.

607 Bolte, S. and Cordelières, F.P. (2006) 'A guided tour into subcellular colocalization analysis in light
608 microscopy', *Journal of Microscopy*, 224(Pt 3), pp. 213–232. Available at: https://doi.org/10.1111/j.1365-
609 2818.2006.01706.x.

610 Briz, V. *et al.* (2017) 'The non-coding RNA BC1 regulates experience-dependent structural plasticity and
611 learning', *Nature Communications*, 8(1), p. 293. Available at: https://doi.org/10.1038/s41467-017-00311-2.

612 Bruining, H. *et al.* (2015) 'Genetic Mapping in Mice Reveals the Involvement of Pcdh9 in Long-Term Social
613 and Object Recognition and Sensorimotor Development', *Biological Psychiatry*, 78(7), pp. 485–495. Available
614 at: https://doi.org/10.1016/j.biopsych.2015.01.017.

615 Bucan, M. *et al.* (2009) 'Genome-wide analyses of exonic copy number variants in a family-based study point
616 to novel autism susceptibility genes', *PLoS genetics*, 5(6), p. e1000536. Available at:
617 https://doi.org/10.1371/journal.pgen.1000536.

618 Buccino, A.P. *et al.* (2020) 'SpikeInterface, a unified framework for spike sorting', *eLife*, 9, p. e61834. Available
619 at: https://doi.org/10.7554/eLife.61834.

620 Canal, F. *et al.* (2011) 'Compartmentalization of the MAPK scaffold protein KSR1 modulates synaptic plasticity
621 in hippocampal neurons', *The FASEB Journal*, 25(7), pp. 2362–2372. Available at:
622 https://doi.org/10.1096/fj.10-173153.

623 Cembrowski, M.S. *et al.* (2016) 'Hipposeq: a comprehensive RNA-seq database of gene expression in
624 hippocampal principal neurons', *eLife*. Edited by E. Marder, 5, p. e14997. Available at:
625 https://doi.org/10.7554/eLife.14997.

626 Clark, L.N. *et al.* (2022) 'Whole genome sequencing identifies candidate genes for familial essential tremor
627 and reveals biological pathways implicated in essential tremor aetiology', *EBioMedicine*, 85, p. 104290.
628 Available at: https://doi.org/10.1016/j.ebiom.2022.104290.

629 Colombo, M.N. *et al.* (2021) 'Comparative 2D and 3D Ultrastructural Analyses of Dendritic Spines from CA1
630 Pyramidal Neurons in the Mouse Hippocampus', *International Journal of Molecular Sciences*, 22(3), p. 1188.
631 Available at: https://doi.org/10.3390/ijms22031188.

632 Curtis, A.J. *et al.* (2023) 'Molecular basis of interactions between CaMKII and α-actinin-2 that underlie dendritic
633 spine enlargement', *eLife*. Edited by T. Saneyoshi, V. Dötsch, and J.W. Hell, 12, p. e85008. Available at:
634 https://doi.org/10.7554/eLife.85008.

635 Duffney, L.J. *et al.* (2013) 'Shank3 Deficiency Induces NMDA Receptor Hypofunction via an Actin-Dependent
636 Mechanism', *Journal of Neuroscience*, 33(40), pp. 15767–15778. Available at:
637 https://doi.org/10.1523/JNEUROSCI.1175-13.2013.

638 Duman, R.S. (2014) 'Pathophysiology of depression and innovative treatments: remodeling glutamatergic
639 synaptic connections', *Dialogues in Clinical Neuroscience*, 16(1), pp. 11–27. Available at:

https://doi.org/10.31887/DCNS.2014.16.1/rduman.

Flaherty, E. and Maniatis, T. (2020) 'The role of clustered protocadherins in neurodevelopment and neuropsychiatric diseases', *Current Opinion in Genetics & Development*, 65, pp. 144–150. Available at: https://doi.org/10.1016/j.gde.2020.05.041.

Giansante, G. *et al.* (2023) 'Neuronal network activity and connectivity are impaired in a conditional knockout mouse model with PCDH19 mosaic expression', *Molecular Psychiatry* [Preprint]. Available at: https://doi.org/10.1038/s41380-023-02022-1.

Goodell, D.J. *et al.* (2017) 'DAPK1 Mediates LTD by Making CaMKII/GluN2B Binding LTP Specific', *Cell Reports*, 19(11), pp. 2231–2243. Available at: https://doi.org/10.1016/j.celrep.2017.05.068.

Gutierrez, M.A., Dwyer, B.E. and Franco, S.J. (2019) 'Csmd2 Is a Synaptic Transmembrane Protein that Interacts with PSD-95 and Is Required for Neuronal Maturation', *eNeuro*, 6(2), p. ENEURO.0434-18.2019. Available at: https://doi.org/10.1523/ENEURO.0434-18.2019.

Hare, B.D. and Duman, R.S. (2020) 'Prefrontal cortex circuits in depression and anxiety: contribution of discrete neuronal populations and target regions', *Molecular Psychiatry*, 25(11), pp. 2742–2758. Available at: https://doi.org/10.1038/s41380-020-0685-9.

Hirano, S. and Takeichi, M. (2012) 'Cadherins in brain morphogenesis and wiring', *Physiological Reviews*, 92(2), pp. 597–634. Available at: https://doi.org/10.1152/physrev.00014.2011.

Hoshina, N. *et al.* (2013) 'Protocadherin 17 Regulates Presynaptic Assembly in Topographic Corticobasal Ganglia Circuits', *Neuron*, 78(5), pp. 839–854. Available at: https://doi.org/10.1016/j.neuron.2013.03.031.

Hutsler, J.J. and Zhang, H. (2010) 'Increased dendritic spine densities on cortical projection neurons in autism spectrum disorders', *Brain Research*, 1309, pp. 83–94. Available at: https://doi.org/10.1016/j.brainres.2009.09.120.

Jiang, Y.-H. and Ehlers, M.D. (2013) 'Modeling autism by SHANK gene mutations in mice', *Neuron*, 78(1), pp. 8–27. Available at: https://doi.org/10.1016/j.neuron.2013.03.016.

Koch, S. *et al.* (2019) 'Atlas registration for edema-corrected MRI lesion volume in mouse stroke models', *Journal of Cerebral Blood Flow and Metabolism: Official Journal of the International Society of Cerebral Blood Flow and Metabolism*, 39(2), pp. 313–323. Available at: https://doi.org/10.1177/0271678X17726635.

Kolberg, L. *et al.* (2023) 'g:Profiler—interoperable web service for functional enrichment analysis and gene identifier mapping (2023 update)', *Nucleic Acids Research*, 51(W1), pp. W207–W212. Available at: https://doi.org/10.1093/nar/gkad347.

Koopmans, F. *et al.* (2019) 'SynGO: An Evidence-Based, Expert-Curated Knowledge Base for the Synapse', *Neuron*, 103(2), pp. 217-234.e4. Available at: https://doi.org/10.1016/j.neuron.2019.05.002.

Kreuz, T. *et al.* (2007) 'Measuring spike train synchrony', *Journal of Neuroscience Methods*, 165(1), pp. 151–161. Available at: https://doi.org/10.1016/j.jneumeth.2007.05.031.

Kristensen, A.S. *et al.* (2011) 'Mechanism of Ca2+/calmodulin-dependent kinase II regulation of AMPA receptor gating', *Nature Neuroscience*, 14(6), pp. 727–735. Available at: https://doi.org/10.1038/nn.2804.

Lee, S. *et al.* (2024) 'Anterior cingulate cortex-related functional hyperconnectivity underlies sensory hypersensitivity in Grin2b-mutant mice', *Molecular Psychiatry* [Preprint]. Available at: https://doi.org/10.1038/s41380-024-02572-y.

Li, M. *et al.* (2010) 'Synaptogenesis in the developing mouse visual cortex', *Brain Research Bulletin*, 81(1), pp. 107–113. Available at: https://doi.org/10.1016/j.brainresbull.2009.08.028.

Lisman, J. *et al.* (2017) 'Viewpoints: how the hippocampus contributes to memory, navigation and cognition', *Nature Neuroscience*, 20(11), pp. 1434–1447. Available at: https://doi.org/10.1038/nn.4661.

Lombardi, W.J. *et al.* (2001) 'Cognitive deficits in patients with essential tremor', *Neurology*, 57(5), pp. 785–790. Available at: https://doi.org/10.1212/wnl.57.5.785.

Luo, R. *et al.* (2012) 'Genome-wide transcriptome profiling reveals the functional impact of rare de novo and recurrent CNVs in autism spectrum disorders', *American Journal of Human Genetics*, 91(1), pp. 38–55. Available at: https://doi.org/10.1016/j.ajhg.2012.05.011.

MacGillavry, H.D. *et al.* (2016) 'Shank-cortactin interactions control actin dynamics to maintain flexibility of neuronal spines and synapses', *The European Journal of Neuroscience*, 43(2), pp. 179–193. Available at: https://doi.org/10.1111/ejn.13129.

Mancini, M., Bassani, S. and Passafaro, M. (2020) 'Right Place at the Right Time: How Changes in Protocadherins Affect Synaptic Connections Contributing to the Etiology of Neurodevelopmental Disorders', *Cells*, 9(12), p. E2711. Available at: https://doi.org/10.3390/cells9122711.

Marshall, C.R. *et al.* (2008) 'Structural variation of chromosomes in autism spectrum disorder', *American Journal of Human Genetics*, 82(2), pp. 477–488. Available at: https://doi.org/10.1016/j.ajhg.2007.12.009.

Mohapatra, A.N. and Wagner, S. (2023) 'The role of the prefrontal cortex in social interactions of animal models and the implications for autism spectrum disorder', *Frontiers in Psychiatry*, 14, p. 1205199. Available at: https://doi.org/10.3389/fpsyt.2023.1205199.

Moretto, E. *et al.* (2018) 'Glutamatergic synapses in neurodevelopmental disorders', *Progress in Neuro-Psychopharmacology and Biological Psychiatry*, 84, pp. 328–342. Available at: https://doi.org/10.1016/j.pnpbp.2017.09.014.

Murru, L. *et al.* (2017) 'Pharmacological Modulation of AMPAR Rescues Intellectual Disability-Like Phenotype in Tm4sf2−/y Mice', *Cerebral Cortex*, 27(11), pp. 5369–5384. Available at: https://doi.org/10.1093/cercor/bhx221.

Murru, L. *et al.* (2021) 'Lateral habenula dysfunctions in Tm4sf2-/y mice model for neurodevelopmental disorder', *Neurobiology of Disease*, 148, p. 105189. Available at: https://doi.org/10.1016/j.nbd.2020.105189.

Pancho, A. *et al.* (2020) 'Protocadherins at the Crossroad of Signaling Pathways', *Frontiers in Molecular Neuroscience*, 13, p. 117. Available at: https://doi.org/10.3389/fnmol.2020.00117.

Pappas, A.L. *et al.* (2017) 'Deficiency of Shank2 causes mania-like behavior that responds to mood stabilizers', *JCI Insight*, 2(20), p. e92052. Available at: https://doi.org/10.1172/jci.insight.92052.

Peça, J. *et al.* (2011) 'Shank3 mutant mice display autistic-like behaviours and striatal dysfunction', *Nature*, 472(7344), pp. 437–442. Available at: https://doi.org/10.1038/nature09965.

Peek, S.L., Mah, K.M. and Weiner, J.A. (2017) 'Regulation of neural circuit formation by protocadherins', *Cellular and molecular life sciences: CMLS*, 74(22), pp. 4133–4157. Available at: https://doi.org/10.1007/s00018-017-2572-3.

Penzes, P. *et al.* (2011) 'Dendritic spine pathology in neuropsychiatric disorders', *Nature Neuroscience*, 14(3), pp. 285–293. Available at: https://doi.org/10.1038/nn.2741.

Poncer, J.C., Esteban, J.A. and Malinow, R. (2002) 'Multiple Mechanisms for the Potentiation of AMPA Receptor-Mediated Transmission by α-Ca2+/Calmodulin-Dependent Protein Kinase II', *Journal of Neuroscience*, 22(11), pp. 4406–4411. Available at: https://doi.org/10.1523/JNEUROSCI.22-11-04406.2002.

Reimand, J. *et al.* (2019) 'Pathway enrichment analysis and visualization of omics data using g:Profiler, GSEA, Cytoscape and EnrichmentMap', *Nature Protocols*, 14(2), pp. 482–517. Available at:

https://doi.org/10.1038/s41596-018-0103-9.

Rice, D. and Barone, S. (2000) 'Critical periods of vulnerability for the developing nervous system: evidence from humans and animal models', *Environmental Health Perspectives*, 108 Suppl 3(Suppl 3), pp. 511–533. Available at: https://doi.org/10.1289/ehp.00108s3511.

Sala, C. *et al.* (2001) 'Regulation of Dendritic Spine Morphology and Synaptic Function by Shank and Homer', *Neuron*, 31(1), pp. 115–130. Available at: https://doi.org/10.1016/S0896-6273(01)00339-7.

Sarowar, T. and Grabrucker, A.M. (2016) 'Actin-Dependent Alterations of Dendritic Spine Morphology in Shankopathies', *Neural Plasticity*, 2016, p. e8051861. Available at: https://doi.org/10.1155/2016/8051861.

Schindelin, J. *et al.* (2012) 'Fiji - an Open Source platform for biological image analysis', *Nature methods*, 9(7). Available at: https://doi.org/10.1038/nmeth.2019.

Schumann, C.M. *et al.* (2004) 'The amygdala is enlarged in children but not adolescents with autism; the hippocampus is enlarged at all ages', *The Journal of Neuroscience: The Official Journal of the Society for Neuroscience*, 24(28), pp. 6392–6401. Available at: https://doi.org/10.1523/JNEUROSCI.1297-04.2004.

Steiner, P. *et al.* (2008) 'Destabilization of the postsynaptic density by PSD-95 serine 73 phosphorylation inhibits spine growth and synaptic plasticity', *Neuron*, 60(5), pp. 788–802. Available at: https://doi.org/10.1016/j.neuron.2008.10.014.

Stuart, T. *et al.* (2019) 'Comprehensive Integration of Single-Cell Data', *Cell*, 177(7), pp. 1888-1902.e21. Available at: https://doi.org/10.1016/j.cell.2019.05.031.

Szklarczyk, D. *et al.* (2019) 'STRING v11: protein-protein association networks with increased coverage, supporting functional discovery in genome-wide experimental datasets', *Nucleic Acids Research*, 47(D1), pp. D607–D613. Available at: https://doi.org/10.1093/nar/gky1131.

Toro, R. *et al.* (2010) 'Key role for gene dosage and synaptic homeostasis in autism spectrum disorders', *Trends in Genetics*, 26(8), pp. 363–372. Available at: https://doi.org/10.1016/j.tig.2010.05.007.

Uemura, M. *et al.* (2022) 'Deficiency of protocadherin 9 leads to reduction in positive emotional behaviour', *Scientific Reports*, 12(1), p. 11933. Available at: https://doi.org/10.1038/s41598-022-16106-5.

Uezu, A. *et al.* (2016) 'Identification of an elaborate complex mediating postsynaptic inhibition', *Science*, 353(6304), pp. 1123–1129. Available at: https://doi.org/10.1126/science.aag0821.

Xiao, X. *et al.* (2018) 'The Gene Encoding Protocadherin 9 (PCDH9), a Novel Risk Factor for Major Depressive Disorder', *Neuropsychopharmacology: Official Publication of the American College of Neuropsychopharmacology*, 43(5), pp. 1128–1137. Available at: https://doi.org/10.1038/npp.2017.241.

Zapata, J. *et al.* (2017) 'Epilepsy and intellectual disability linked protein Shrm4 interaction with GABABRs shapes inhibitory neurotransmission', *Nature Communications*, 8, p. 14536. Available at: https://doi.org/10.1038/ncomms14536.

Zhang, Y. *et al.* (2024) 'Nuclear translocation of cleaved PCDH9 impairs gastric cancer metastasis by downregulating CDH2 expression', *iScience*, 27(2), p. 109011. Available at: https://doi.org/10.1016/j.isci.2024.109011.

Zhong, J. *et al.* (2009) 'BC1 regulation of metabotropic glutamate receptor-mediated neuronal excitability', *The Journal of Neuroscience: The Official Journal of the Society for Neuroscience*, 29(32), pp. 9977–9986. Available at: https://doi.org/10.1523/JNEUROSCI.3893-08.2009.

Zhou, Y. *et al.* (2019) 'Metascape provides a biologist-oriented resource for the analysis of systems-level datasets', *Nature Communications*, 10(1), p. 1523. Available at: https://doi.org/10.1038/s41467-019-09234-6.

FIGURES LEGENDS

Figure 1. PCDH9 is enriched at glutamatergic synapses and its expression peaks in the first postnatal weeks in the hippocampus

A Representative PCDH9 western blot of brain regions and body organs from 2-month-old wild-type mice. Two PCDH9 isoforms at ~130 kDa and ~180 kDa are detected, as previously reported (Bruining *et al.*, 2015). OB, olfactory bulb. PFC, prefrontal cortex. **B** Quantifications of PCDH9 levels from (A). Protein levels were normalized to GAPDH. n=4. Kruskal-Wallis test, no significant differences. n.d., not detected. **C** Representative PCDH9 western blot on hippocampus from wild-type mice at different ages. E18, embryonic day 18; P3-180, postnatal day 3-180. **D** Quantifications of PCDH9 levels from (C). Protein levels were normalized to GAPDH. Mean with SEM is represented. n=3. Kruskal-Wallis test, **p<0.01. **E** Representative PCDH9 western blot on cortex from 2-month-old wild-type mice. n=2. S2, supernatant 2 (cytosol-enriched fraction). P2, pellet 2 (membrane-enriched fraction). PSD95 and ACTIN are used as markers of P2 and S2, respectively. **F** Representative confocal images of DIV18 rat hippocampal neurons co-immunostained for PCDH9 and synaptic markers VGLUT1, VGAT, PSD95, GEPHYRIN. Insets show higher magnification of a dendrite. n=3 independent cultures. **G** Mander's coefficient quantification of PCDH9 puncta colocalizing with presynaptic (top) and postsynaptic (bottom) markers analyzed in (F). VGLUT1, VGAT, n=13 neurons. Mann-Whitney test, ****p<0.0001. PSD95, HOMER1, GEPHYRIN, n=17-27 neurons. Kruskal-Wallis test, *p<0.05. **H** Pearson coefficient quantification of PCDH9 signal colocalizing with presynaptic (upper) and postsynaptic (bottom) markers analyzed in (F). VGLUT1, VGAT, n=13 neurons. Mann-Whitney test, ***p<0.001. PSD95, HOMER1, GEPHYRIN, n=17-27 neurons. Postsynaptic markers, Kruskal-Wallis test, ****p<0.0001. See Figure 1-1 for more details.

Figure 2. *Pcdh9* deletion leads to aberrant presynaptic and postsynaptic compartments in the CA1

A Representative electron micrographs of pyramidal neurons synapses from the dorsal CA1 of 2-month-old WT and *Pcdh9* KO mice. Scale bar, 100 nm. **B** Quantifications of synaptic features from (A). n=30-50 synapses from 2 mice per genotype. The horizontal solid line across the violin plot represents the median, and the two dotted lines indicate the quartiles. Mann-Whitney test, *p<0.05, **p<0.01. **C** Representative electron micrographs of pyramidal neurons synapses from the vmPFC layer V-VI of 2-month-old WT and *Pcdh9* KO mice. Scale bar, 100 nm. **D** Quantifications of synaptic features from (C). n=50-70 synapses from 2 mice per

genotype. The horizontal solid line across the violin plot represents the median, and the two dotted lines indicate the quartiles. Mann-Whitney test, no significant differences. **E** Representative western blot (left) and corresponding quantification (right) of synaptic markers levels on hippocampus from 2-month-old WT and *Pcdh9* KO mice. n=8-15 mice per genotype. Mann-Whitney test, no significant differences. **F** Representative western blot (left) and corresponding quantification (right) of synaptic markers levels on cortices from 2-month-old WT and *Pcdh9* KO mice. n=6-9 mice per genotype. Mann-Whitney test, no significant differences. See Figure 2-1, 2-2 and Table 2-1 for more details.

Figure 3. *Pcdh9* deletions induces the dysregulation of key synaptic genes and the broad up-regulation of the synaptic transcriptome in the CA1

A UMAP plots of snRNA-seq data. 16833 nuclei from WT and *Pcdh9* KO hippocampi were grouped into 46 different clusters and colored based on the attributed cell type. n=2 mice per genotype. **B** UMAP plots of snRNA-seq data, with nuclei colored based on the combined expression levels of CA1 markers. The numbers of the clusters identified as CA1 are in blue. **C** Heatmap of CA1 markers fold changes among the different clusters. Clusters identified as CA1 populations are enclosed in a rectangle. **D** Volcano plots showing the KO/WT fold change and p-value distributions of genes in CA1 cluster 5 (top), 6 (center) and 13 (bottom). Up-regulated and down-regulated DEG are colored in green and red, respectively. **E** Network visualization of the combined 31 DEG found in CA1 clusters 5, 6 and 13. Each node represents a gene and is colored based on its function. A line connecting two nodes indicate a physical or functional interaction, as analyzed with STRING. The line thickness indicates the strength of data support. **F** The 4 GO categories (biological processes) identified with gProfiler on CA1 DEG are represented. Green and red indicate up- and down-regulated DEG, respectively. For each GO category, the statistical significance and the associated genes are represented (brown square, inferred from experiments; orange square, inferred from sequences). **G** The 3 synaptic GO categories identified with SynGO on CA1 DEG. For each GO category, the statistical significance and the associated genes are indicated. **H** Representative confocal images of CA1 neurons from 3-month-old WT and *Pcdh9* KO mice, immunostained for MAP2 (neuronal marker) and CORTACTIN or SHANK2. Scale bar, 20 µm. **I** Quantification of CORTACTIN (top) or SHANK2 (bottom) puncta fluorescence intensity from (H). n=8-12 sections from 3-4 mice per genotype. Mann-Whitney test, *p<0.05. **J** The effect of *Pcdh9* deletion on the expression levels of non-synaptic, presynaptic and postsynaptic genes in cluster 5 (top left), 6 (top rigth) and

13 (bottom) is shown. The horizontal line across the violin plot represents the median. Kruskal-Wallis test, ****p<0.0001. See Figure 3-1, 3-2 and Table 3-1, 3-2, 3-3, 3-4 and 3-5 for more details.

Figure 4. *Pcdh9* deletion leads to increased frequency of EPSCs and reduced network activity in the CA1

A Representative traces of mEPSCs recorded from WT and *Pcdh9* KO CA1 pyramidal neurons. **B** Quantification of amplitude, decay time, area and frequency of mEPSCs from (A). Mean with SD is represented. n=16-17 recorded neurons from 5 independent animals per genotype. Mann-Whitney test, *p<0.05. **C** Representative traces of mEPSCs recorded from vmPFC pyramidal neurons from WT and *Pcdh9* KO mice. **D** Quantification of amplitude, decay time, area and frequency of mEPSCs from (C). Mean with SD is represented. n=21-22 recorded neurons from 5 independent mice per genotype. The horizontal line across the plot represents the mean. Mann-Whitney test, no significant differences. **E** Quantification of paired pulse ratio experiments in CA1 pyramidal neurons from WT and *Pcdh9* KO mice. n=5 independent mice per genotype. Mann-Whitney test, no significant differences. **F** Quantification of CA1 fEPSP slope before and after HFS from WT and *Pcdh9* KO mice. n=5 independent mice per genotype. Mann-Whitney test, no significant differences. **G** Representative MEA recordings from WT and *Pcdh9* KO hippocampal slices. **H** Representative raster plots showing CA1 electrical activity recorded from 100 channels over 2 minutes (top), and representative traces recorded from a single channel positioned in the CA1 (bottom), showing reduced firing activity in *Pcdh9* KO mice. **I** Quantification of firing rate, burst activity, number of spikes per burst and burst duration from MEA recordings for each hippocampal subregion in WT and *Pcdh9* KO genotypes. The horizontal line across the box plot represents the mean. n=4-6 independent mice per genotype. Mann-Whitney test, **p<0.01. **J** Synchronization index of the CA1 subregion in WT and *Pcdh9* KO genotypes. Mean with SEM is represented. n=3-6 independent mice per genotype. Mann-Whitney test, *p<0.05. See Figure 4-1 for more details.

Figure 5. *Pcdh9* ablation leads to aberrant transcriptional profile, morphology and function of CA1 excitatory synapse, and defective CA1 network activity. *Pcdh9* deletion causes synaptic dysregulation at multiple levels, transcriptional (key synaptic genes alterations and widespread up-regulation of the synaptic

850 transcriptome), morphological (presynaptic terminal and PSD overgrowth) and functional (increased mEPSCs
851 frequency), and results into impaired network activity in the CA1.

852

853

Figure 1

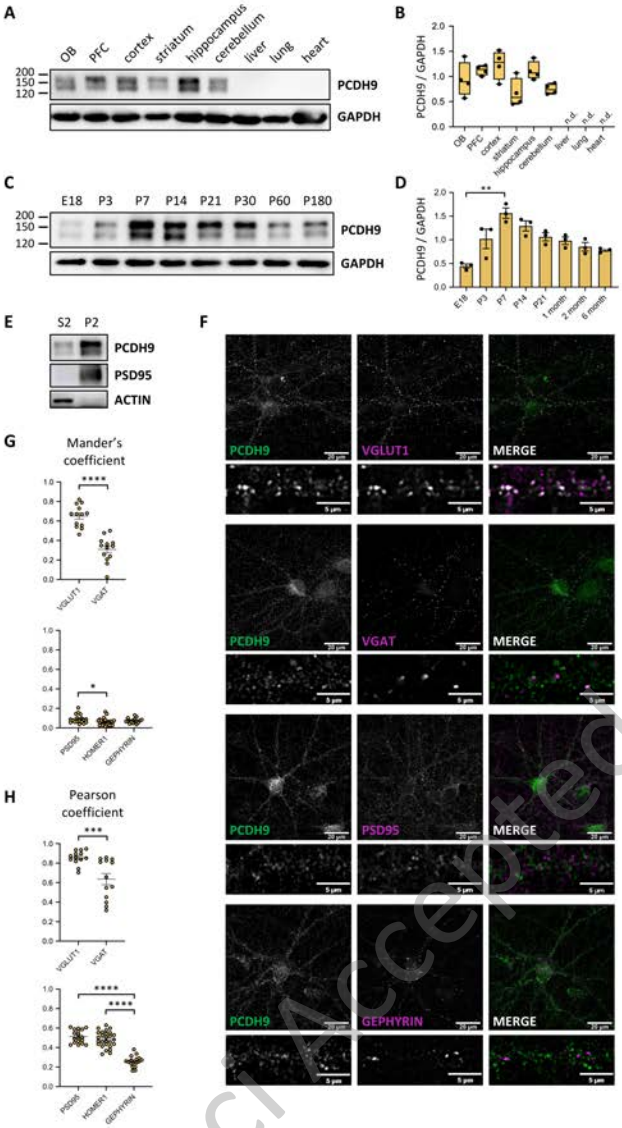

Figure 2

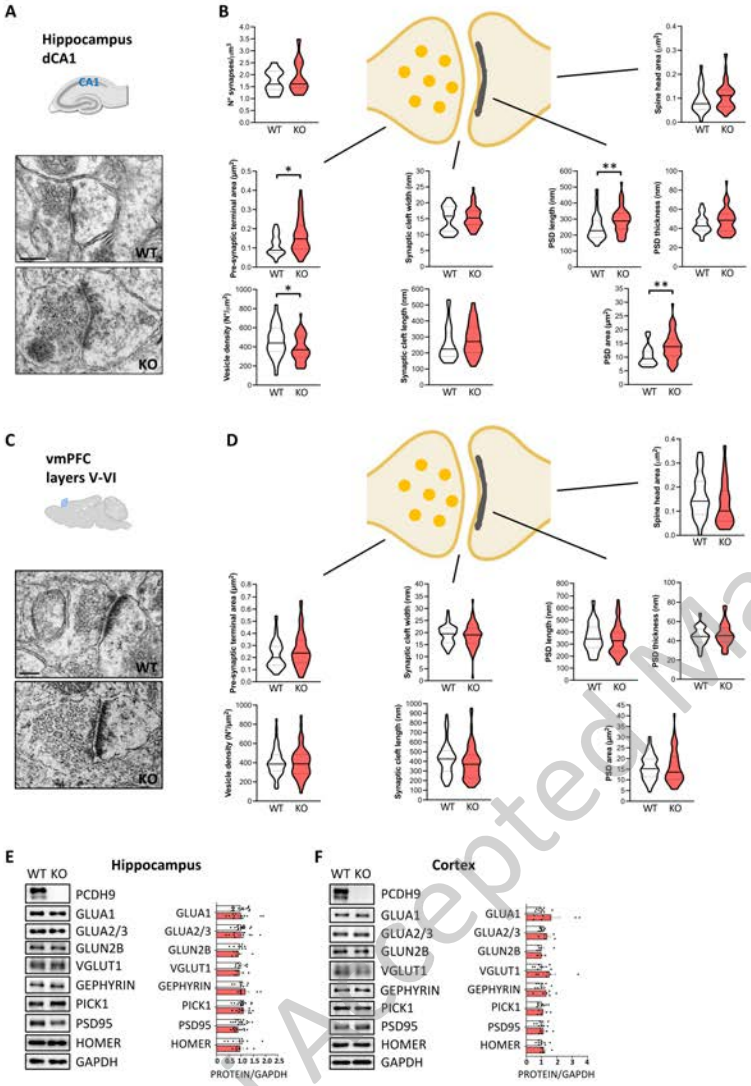

Figure 3

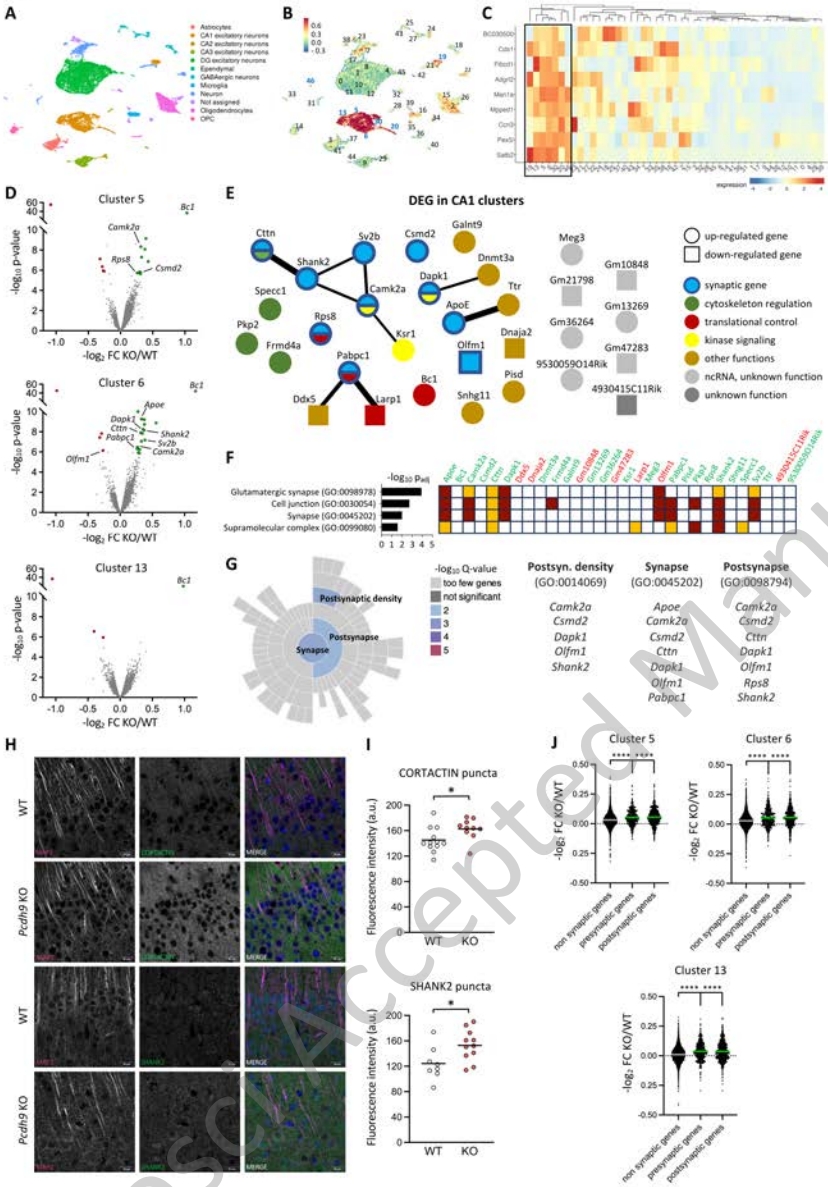

Figure 4

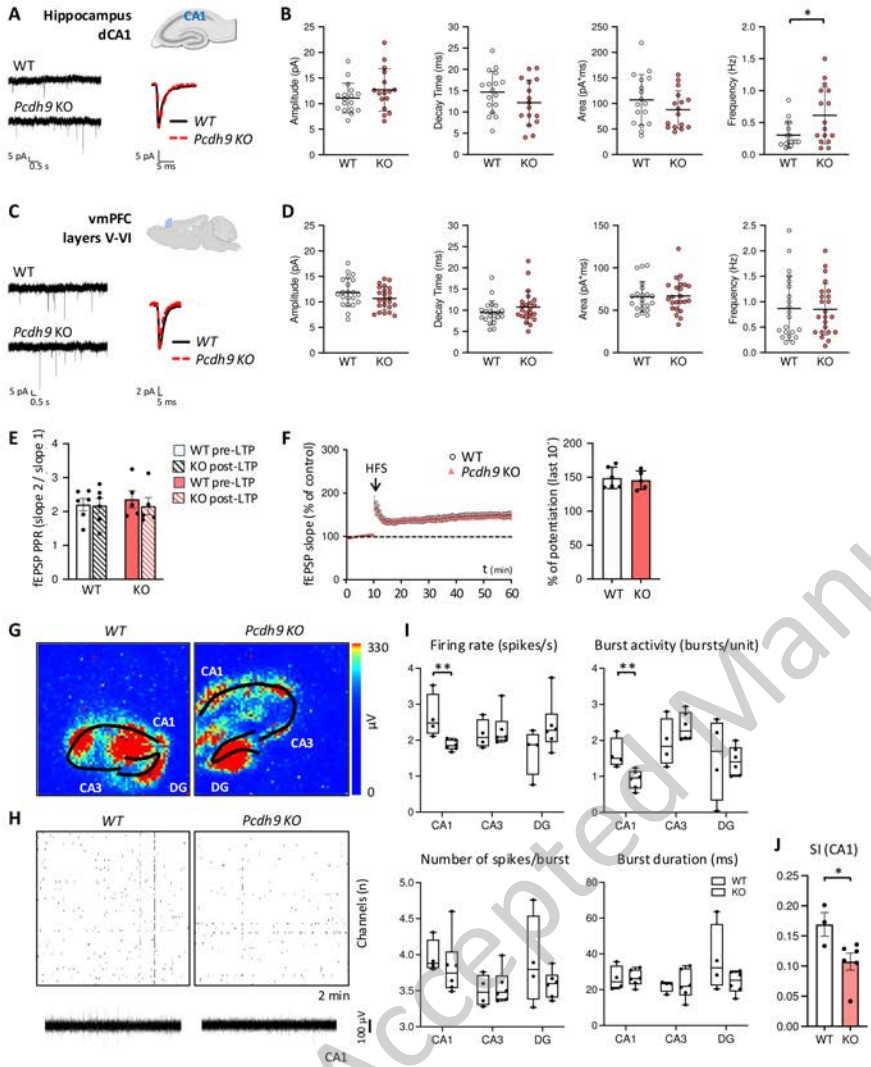

Figure 5